

Contour Extraction and Quality Inspection for Inner Structure of Deep Hole Components

Xin-Yi Gong, Hu Su, De Xu, *Senior Member, IEEE*, Hua-Bin Yang, Zheng-Tao Zhang, and Lei Zhang

Abstract—The paper focuses on the contour extraction for the inner wires of a kind of deep hole component to achieve a high-accuracy inspection. The vision system consisting of a camera and an endoscope is developed to acquire high-quality images of the internal structure. For the acquired images, a contour extraction method is proposed, which could be divided into the following steps. Firstly, the start points of wires referred as the prior information on the component are obtained with a predefined filter, and on the basis, several regions of interest (ROIs) are defined. Secondly, the multiscale probability of boundary (mpb) operator is utilized to detect edges in the ROIs. Thirdly, a Brownian motion model is established to calculate the connectivity between edges. The prior information obtained previously is used again to determine the probabilities of the edges belonging to the contours. Finally, the symmetric ratio contour (SRC) method is used to form the wires' contours with the edges. In the proposed method, the edges belonging to the wires' contours are enhanced by making full use of the prior information, resulting in the improvement in accuracy and real-time performance. As evidenced by the experiments, the proposed method can efficiently extract the inner wires' contours from the component's image with low contrast conditions, noises and shadows.

Index Terms—Brownian motion, edge grouping, contour extraction, deep-hole component

I. INTRODUCTION

The component shown in Fig. 1 is an electronic connector called spring-wire socket which has found an increasingly wide utilization in the fields of aerospace, navigation and military industry due to their distinct merits, like low wear and tear, long life, and high reliability in a strong vibration shock environment. The component includes two parts: a small diameter body and an inner sleeve with deep aperture. The integrity of the internal structure of the aperture directly affects its conductive property and needs to be strictly inspected[1]. Therefore, the morphological information of the internal structure should be accurately extracted and its contour should be detected precisely. However, as can be seen from the figures, the inspection would be a difficult task even for experienced

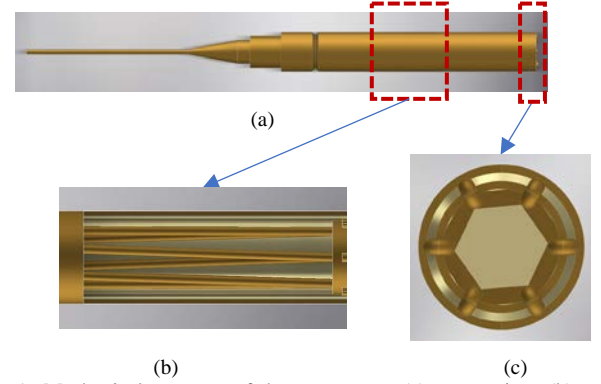


Fig.1 Mechanical structure of the component, (a) stereo view, (b) partially-sectioned view, (c) cross-section view.

workers due to the small diameter and deep hole. In order to inspect the components more efficiently and accurately, it is essential to contrast an automatic optical inspection systems which is widely used in modern electronic industries [2, 3]. Aiming to achieve automatic inspection of the component, the paper focuses on how to extract the contours of the inner wires robustly and accurately which is the most vital step of the inspection.

Contour detection [4] has been intensively studied in the past decades. Early approaches locate discontinuities in image brightness, such as Sobel, Prewitt and Canny operators [5]. However, Martin et. al [6] pointed out that this was an inadequate model due to textures and noises. In view of this limitation, a probabilistic detector named probability of boundary (Pb) was proposed in [6] in which color, brightness and texture gradients were combined to improve the detection accuracy. Except for the features constructed in [6], Ren et. al [7] defined localization and relative contrast features. Subsequently, they suggested Sparse Code Gradients (SCG) features in [8] to replace the hand-designed gradient features in [6]. Note that the SCG features were automatically learned from image data through sparse coding, and thus human effort was minimized. In addition to these local features, global information has also been made use of in contour detection [9, 10, 11]. The methods [12-15] regarded contours as boundaries of interesting regions. Although effective, the methods are invalid for contours that do not arise from region boundaries.

Due to the small aperture and the complex structure of the component, it is hard to get satisfactory images. Shadows and noises are almost inevitable in the image and the con-

Manuscript received June 8, 2018. This work was supported in part by the National Natural Science Foundation of China under Grants 61503378, 61473293, 61733004 and 61421004, and by the Project of Development in Tianjin for Scientific Research Institutes Supported by Tianjin Government (16PTYJGX00050).

All authors are with the Research Center of Precision Sensing and Control, Institute of Automation, Chinese Academy of Sciences (CASIA), Beijing 100190, China, and also with the University of Chinese Academy of Sciences, Beijing 101408, China. D. Xu is also with Tianjin Intelligent Technology Institute of CASIA Co., Ltd. (e-mail: zhengtao.zhang@ia.ac.cn).

trast of the image is relatively low. Contours often break into fragments and cannot be completely detected even using the most sophisticated detector. We consider contour grouping and completion methods as solutions to the problem. The grouping process collects individual edges together to form continuous contours. In [16], a general grouping approach was proposed which could be used for the grouping of various types of measurements, and to incorporate different grouping cues. In [17], the concepts of link saliency and contour saliency were introduced and used to identify smooth closed contours bounding objects of unknown shape in real image. In [17], the method, named as stochastic completion fields [18, 19], was adopted in the calculation of transition probabilities. Besides, based on the optimization framework pioneered by Jermyn and Ishikawa [20], the method called ration contour was presented in [21, 22] for extracting salient region boundaries. In [23], the path-based grouping method was proposed, in which connectivity of edge elements via mediating elements was sufficiently explored. With these methods, the accuracy requirement in contour detection could be relaxed. However, in many of the approaches, global optimization needs to be performed which is intractable and is impractical due to high computational complexity even if the problem could be formally solved.

In this paper, the contour extraction for the inner wires of the component shown in Fig. 1 is investigated. To make the further inspection efficiently, the completeness of the extracted contour need to be guaranteed. However, it is not an easy task due to the disturbances and low contrast in the images. Inspired by the stochastic completion fields [17, 18], a hierarchical Brownian motion model is established to calculate the adjacent probability of the edges. Compared to the original method, the proposed model is more suitable to the discrete points in images. Then, inheriting the path-based idea in [22], the probabilities of edges belonging to the contours are determined based on the endpoints of the wires. The edges having high probabilities are enhanced and those arising from the noises, shadows and textures are thus suppressed, in which way the computational complexity could be improved. In addition, a curve smoothing algorithm is introduced to obtain more accurate curvature statistics of the wires' shapes to determine the parameters involved in Brownian motion model. The detected endpoints and the curvature statistics of the wires constitute prior information which are sufficiently explored to overcome the difficulties in contour extraction. This can also be viewed as the difference between our method with previous ones. The contributions of the paper could be summarized as follows. Firstly, an automatic image acquisition system is developed to produce high-quality images. Secondly, prior information is made full use of for efficiency improvement, in which a curve smoothing algorithm is mentioned. Finally, a contour extraction method is proposed which could overcome the disturbances to guarantee to completeness of the contours.

The remainder of this paper is organized as follows. Section II introduces the image acquisition system. A detailed account of image preprocessing is provided in Section III. In Section IV, hierarchical Brownian motion is introduced and is used to model to the probability of the edge belonging to the contour.

Then, the proposed contour extraction and quality inspection method is summarized in Section V and Section VI presents the experimental results. Finally, the paper is concluded in Section VII.

II. IMAGE ACQUISITION

The component is conus-like with external diameter of 1.1mm and height of 15mm. The component contains several copper wires each of which is 0.12mm in diameter. The wires are evenly distributed along the 5mm-depth hole and cover from the top to the bottom. Considering the unique nature of the component, an effective scheme of image acquisition is designed, as illustrated in Fig. 2. In the scheme, the endoscope replaces the conventional lens and light source, in order to overcome the non-uniform luminance diffusion caused by traditional lighting method. The endoscope has three translational degrees of freedom to adjust the distance between the endoscope and the component in X-, Y- and Z- directions, respectively. In addition, the component rotates around the Y- and Z- directions to make the component and the optical axis of the endoscope be consistent.

To obtain stable and high-quality image, several important parameters are experimentally determined. For convenience expression, some notations are firstly introduced. As illustrated in Fig. 2, the distance of the component and the endoscope is Δ_1 . The axis of the component is denoted as l_c while that of the endoscope is l_e . The distance and angle between l_c and l_e are respectively denoted as Δ_2 and α . From experiments, we found

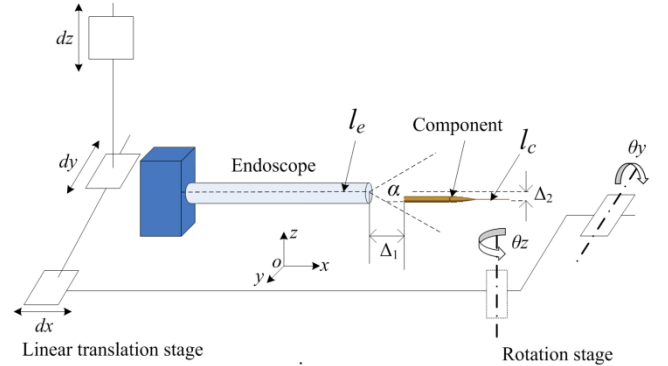


Fig. 2 Hardware configuration of the image acquisition system.

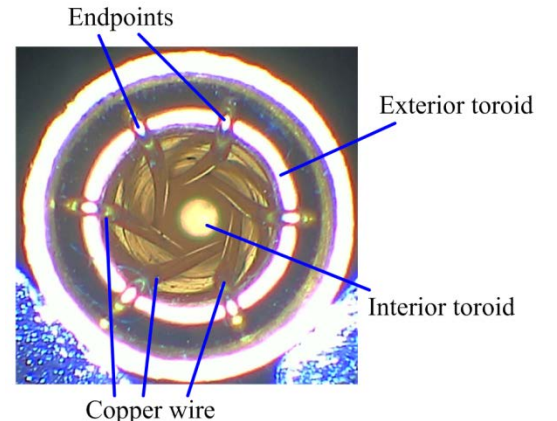


Fig. 3 The component

that Δ_1 should be about 1mm and Δ_2 should be no more than 0.6mm. And the angle α should be less than $\pm 10^\circ$. Using the system, the obtained image is shown in Fig. 3. As illustrated, the toroid intersecting with the wires is referred as exterior toroid. The toroid at the center of the image is referred as interior toroid. Both the toroids have high brightness. These prior knowledges should be sufficiently considered to improve the detection efficiency.

III. IMAGE PREPROCESSING

As can be seen from Fig. 3, the advent of noises and shadows would make accurate extraction of the wires' contours far more challenging. Prior knowledge would be helpful to overcome the difficulty, which, in particular, refers to two toroids having high brightness, one of which is at the center of the image and the other of which intersects the wires. The intersections which also are the endpoints of the wires could be determined by a filter. Then, the ROIs are isolated from the image, each of which bounds a single whole wire and meanwhile is the smallest in area. Edge detection and contour extraction are conducted independently for each ROI. In this way, the number of edges is significantly reduced and the computational complexity is thus improved.

A. ROI Isolation

For each of the wires, the ROI is firstly determined. As observed, a wire generally starts from the endpoint on the exterior toroid and extends to the interior toroid which is at the center of the component. Regarding them as two non-adjacent vertexes of a rectangle, the ROI could be straightforwardly determined. Based on the above analysis, the following strategy is designed with which the ROIs, one for each wire, could be eventually recognized.

Note that exterior toroid is quasi-circular with high brightness. Its feature points are extracted by inside-out seeking in the image. Fitting the points with the least square method, mathematical expression of the exterior toroid is approximately calculated. The following is to search the endpoints on the exterior toroid. It is found from Fig. 3 that, on the exterior toroid, the gray values at the sides of the endpoints are much smaller than those of the rest. In response to this situation, a detector template is designed as shown in Fig. 4. In the template, the weights setting to 1 correspond to the endpoint and the exterior toroid while those setting to -1 correspond to the edges of the endpoint. The template is convoluted with the image at each point on the exterior toroid. The normalized convolution result S_i is calculated as

$$S_i = \sum_{k=-6}^6 I_{i+k,j} \cdot W(k) \quad (1)$$

where W is the weight of template, $I_{i,j}$ is the gray value of the pixel in i -th row and j -th column of the image. The convolution results at the endpoint would be much bigger than those at other points. With the predefined threshold T_1 , whether a point is the endpoint or not is determined. According to the endpoints and the interior toroid, the ROIs are recognized and isolated from the original image. And the effect of disturbance outside the

ROIs can thus be eliminated.

+1	-1	-1	-1	+1	+1	0	+1	+1	-1	-1	-1	+1
----	----	----	----	----	----	---	----	----	----	----	----	----

Fig. 4 The detector template

B. Edge Detection

For each ROI, edge detection is carried out by using the mpb detector [9, 10]. The detector appropriately combines a set of brightness, color, texture cues at multiple scales to improve the detection accuracy. It models the true probability of a boundary at every image location and orientation. A comparison is made among the mpb, Canny, LoG and Sobel operators. The results are presented in Fig. 5. Figs. 5(b), 5(c), 5(d) and 5(e) respectively show the results achieved by these detectors. It can be seen that the mpb operator can overcome the effect of noises and shadows while more edge information is obtained.

Then, each detected edge is approximated by straight line segments. We segment the edge by recursively breaking the edge at the point maximally distant the straight line connecting its endpoints. Subdivision terminates when the distance from the straight line to every point on the edges is less than a threshold T_2 . We discard all the edges whose length is less than T_3 pixels because it is difficult to derive accurate tangent and curvature information from short noisy edges. Without introducing chaos, the edges mentioned in the following are all refer to the straight lines segmented from the original edges.

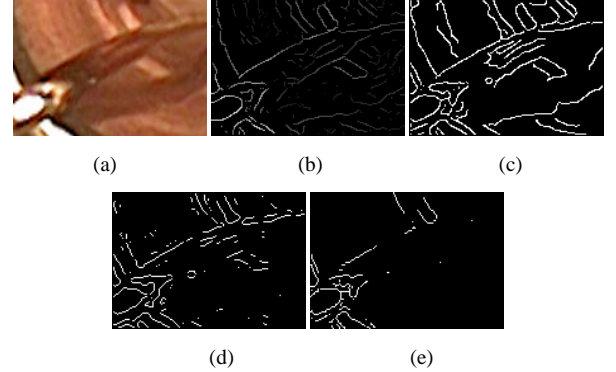


Fig. 5 Detection results using different operators, (a) original image, (b) mpb, (c) Canny, (d) LoG, (e) Sobel.

IV. CONNECTIVITY MODELING

A. Brownian Motion Model

Connectivity is a property defined for pairs of edges. High connectivity means that the two edges are close together and can be smoothly interpolated. That is, proximity and continuation have direct impacts on the connectivity. To quantify the connectivity reasonably, we model proximity and continuation by a particle moving with constant speed in directions undergoing Brownian motion [16]. Three parameters control the motion. The change in direction which only influences the curvature of the curve traced by the particle models the principle of good continuation. The decay rate associates the length of the curve, representing the distance over which the edges are likely to be linked. Hence, it models proximity. The speed

represents the scale at which the scene is analyzed and thus is closely relevant to both the curvature and the length of the curve. It models both proximity and continuation. Here, we assume that, the change in direction obeys Gaussian distribution. A fixed speed is chosen which performs well in experiments. The process of Brownian motion can be represented as

$$\begin{cases} \dot{x} = v \cdot \cos \theta \cdot \tau \\ \dot{y} = v \cdot \sin \theta \cdot \tau \\ \dot{\theta} \sim N(\bar{m}, \delta^2) \end{cases} \quad (2)$$

where \dot{x} and \dot{y} specify change in position. v is the speed of the particle. τ is the decay rate which sets a limit to the distance the particle moves. Note that a segmented ROI tightly surrounds the wire. Here, τ is set to 1, meaning that each edge in the ROI might be on the contour of the copper wire. θ is the change in direction, which stands for the variation in orientation (*i.e.* curvature) of two edges and we consider it obeying the Gaussian distribution $N(\bar{m}, \delta^2)$.

To make the motion model more suitable for discrete pixels in image, a hierarchical propagation strategy is developed and utilized. In the strategy, suppose that, the initial position of the particle forms 0 layer denoted as O_0 . The eight neighbors, or simply neighbors for short in the following, are uniformly called as 1st layer denoted as O_1 . Generally, with k -th layer O_k , O_{k+1} is expressed as

$$O_{k+1} = C_I \left(\bigcup_{j=0}^k O_j \right) \cap E(O_k) \quad (3)$$

where $E(A) = \{\cup_i E(a_i) | a_i \in A\}$, $E(a_i)$ is the set of the neighbors of a_i . I represents the whole image and $C_I(A)$ is the complementary set of A in I . The moving of the particle from 0 to k -th layer is completed step by step where, in each step, it moves from n -th layer to the neighbors on the $n+1$ -th layer. The strategy is illustrated in Fig. 6.

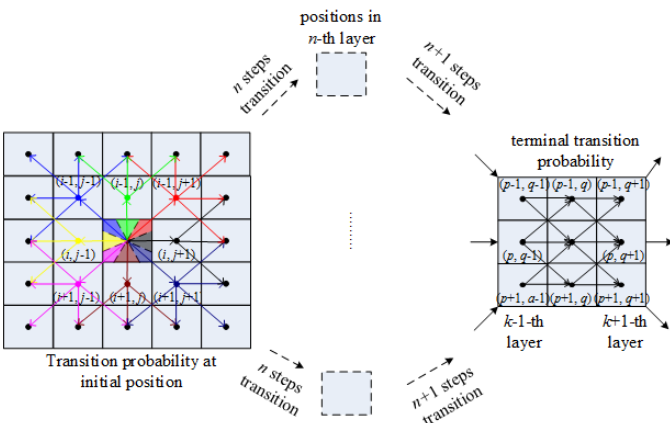


Fig. 6 Transition probability of the Brownian motion.

Given initial and terminal positions, Brownian motion is carried out. Before proceeding, we explain several notations. The initial position and direction are denoted as P_0 and θ_0 , respectively. The terminal position and direction are P_e and θ_e . In the motion, P_e is supposed to be in k -th layer. One certain

position located in n -th layer is generally represented as P_n while its moving direction is θ_n . Its neighbors are labeled as P_{ni} , $i=1, 2, \dots, 8$. $l(\cdot)$ is the layer in which the position locates. The change of the moving direction is $\Delta\theta$ which obeys the Gaussian distribution in (2). For the particle moving from P_n , the next to arrive is

$$P^* = \underset{P_{ni}}{\operatorname{argmin}} \left\| \theta(\overrightarrow{P_n P_{ni}}) - (\theta_n + \Delta\theta) \right\| \quad (4)$$

where $\theta(\cdot)$ represents the inclined angle of the vector. Subsequently, the particle would proceed next movement step at P^* in the direction $\theta(\overrightarrow{P_n P^*})$. Based on the above definitions, the transition probabilities of one-step, N -step and terminal are respectively constructed, which form the basis of the calculation of probability that the particle moving from the initial position to the terminal position.

One-step transition probability. It refers to the probability of a particle moving from current position to each of its eight neighbors. Based on (4), the transition probability $Pr(P_{ni}|P_n, \theta_n)$ of the particle moving from P_n in the direction θ_n to P_{ni} is computed as

$$Pr(P_{ni}|P_n, \theta_n) = \int_{\theta(\overrightarrow{P_n P_{ni}}) - \pi/8 - \theta_n}^{\theta(\overrightarrow{P_n P_{ni}}) + \pi/8 - \theta_n} N(\theta; \bar{m}, \delta^2) d\theta \quad (5)$$

N -step transition probability. It refers to the probability that the particle moves from P_0 to P_n in n -th layer ($k-1 \geq n \geq 2$). In the moving procedure from $n-1$ -th to n -th layer, the particle walks along one or more paths, arriving at the same position, as illustrated in Fig. 6. In the figure, different colored arrows represent different paths and the intersections imply that more than one paths could reach the position. Moreover, it is also found that n -th layer can only be reached by $n-1$ -th layer. Therefore, the probability calculation is only concerned with the paths that pass through $n-1$ -th layer. Based on one-step transition probability, N -step transition probability $Pr(P_k)$ can be computed as

$$Pr(P_n) = \sum_{P_c \in E(P_n) \cap O_{n-1}} Pr(P_c) \cdot \int_{\theta(\overrightarrow{P_c P_n}) - \pi/8 - \theta_c}^{\theta(\overrightarrow{P_c P_n}) + \pi/8 - \theta_c} N(\theta; \bar{m}, \delta^2) d\theta \quad (6)$$

Terminal transition probability. It refers to the probability that the particle moves from P_0 to P_e in k -th layer. Considering the directions of the particle at P_0 and P_e and using the results in (5) and (6), the probability $Pr(P_e)$ is represented as

$$Pr(P_e) = \sum_{P_c \in E(P_e) \cap O_{k-1}} Pr(P_c) \int_{\theta(\overrightarrow{P_c P_e}) - \pi/8 - \theta_c}^{\theta(\overrightarrow{P_c P_e}) + \pi/8 - \theta_c} d\theta' N(\theta'; \bar{m}, \delta^2) N(\theta; \bar{m}, \delta^2) \quad (7)$$

The probabilities computed with (5), (6) and (7) are used to measure the connectivity between any two edges. Moreover, to facilitate the next calculation, self-connectivity is set to 0. Then, we construct a matrix S to describe the connectivity relation of the edges in the image. In the matrix, the element s_{ij} represents



Fig. 7 Curvature estimation, (a) human marked image, (b) corresponding curvatures

the connectivity between edge i and edge j and the number of rows (columns) equals to that of the edges detected in the image. Obviously, $e_{ij} = e_{ji}$ and $e_{ii} = 0$. Therefore, S is symmetric and all elements on the primary diagonal are 0s.

B. Path-Based Connectivity Probability Calculation

This section considers the probabilities of the detected edges belonging to the contour with the endpoint as prior marker. For each edge, the probability is modeled as the connectivity to the endpoint, which, however, is different from the one introduced in the previous section. The former stresses the connectivity via a sequence of intermediate edges while the latter favors high mutual similarity. The connectivity should be mediated by peer edges along the contour, no matter how large the extend may be. In order to emphasize their difference, we propose the concept of path-based connectivity. As analyzed, this concept concerns the path constituted of intermediate edges and could be computed by the connectivity of each two consecutive edges on the path. Incorporating the prior information with the work of Fischer [22], the path-based connectivity is computed as

$$D_i = \max_{\Gamma_p \in \text{Path}(E_i, E_0)} \max\{Pr_0(E_i), \min_{1 \leq e < |\Gamma_p|} S_{\Gamma_p[e]\Gamma_p[e+1]}\} \quad (8)$$

where E_0 and E_i are the endpoint and edge in the image, respectively. D_i is the path-based connectivity of E_i which represents its probability of belonging to the contour. $\text{Path}(E_i, E_0)$ is the set of paths from E_0 to E_i and Γ_p is one of the paths. $Pr_0(E_i)$ is the connectivity between E_i and E_0 , which is calculated with the method described in the previous section. S is the connectivity matrix. (8) means that, the path-based connectivity could be measured by the larger of $Pr_0(E_i)$ and the lowest connectivity of the path Γ_p^* , where Γ_p^* is the path with maximum lowest connectivity out of the set of all admissible paths between E_i and E_0 .

C. Empirical Determination of Parameters in Brownian Motion

Considering the high consistency of contour shapes of the wires, we begin with a study of the statistical properties with a number of human marked images, as shown in Fig. 7(a). In the marked images, we trace out the segment contours and numerically estimate the curvatures of each point. Fig. 7 provides an example of curvature estimation. Fig. 7(b) illustrates curvatures of the corresponding points in Fig. 7(a), the brighter the pixel in Fig. 7(b) is, the bigger the curvature of the corresponding pixel in Fig. 7(a) has. Fig. 7 indicates that the points

in Fig. 7(a) corresponding to those in the red ellipse in Fig. 7(b) have big curvatures. However, this disaccords with human experience. Intuitively, this should be caused by noises and coordinate jumps between discrete points. To eliminate the effects, curve smoothing is required for accurate curvature estimation.

By optimizing the work of Wang [20], a global optimized algorithm is proposed to smooth the curves which are originally represented by a number of points obtained by edge detection. We refer to these points as *base points* and associate a quadratic spline to each of them. The curves could then be represented with a set of connected quadratic splines. Suppose that, P_i is the i th base point whose coordinate is (x_i, y_i) . P_{i-1} and P_{i+1} are adjacent to P_i , and the coordinates are (x_{i-1}, y_{i-1}) and (x_{i+1}, y_{i+1}) , respectively. Interpolating the P_i , P_{i-1} and P_{i+1} with quadratic curve, the spline for the i -th base point has the following parametric form

$$s_i: \begin{pmatrix} x(t) \\ y(t) \end{pmatrix} = \begin{pmatrix} x_i \\ y_i \end{pmatrix} + \begin{pmatrix} a_i & b_i \\ c_i & d_i \end{pmatrix} \begin{pmatrix} t^2 \\ t \end{pmatrix} \quad (9)$$

Substituting $t = 0$ into Eq. (9), we can get $s_i(0) = P_i$ and both P_{i-1} and P_{i+1} are on the spline. Setting $s_i(-1) = P_{i-1}$ and $s_i(1) = P_{i+1}$, then we have

$$\begin{cases} a_i = \frac{1}{2}(x_{i+1} + x_{i-1}) - x_i, b_i = \frac{1}{2}(x_{i+1} - x_{i-1}) \\ c_i = \frac{1}{2}(y_{i+1} + y_{i-1}) - y_i, d_i = \frac{1}{2}(y_{i+1} - y_{i-1}) \end{cases} \quad (10)$$

Considering the overlap in positions of the adjacent splines s_i , s_{i-1} and s_{i+1} , the constraints $s'_i(t=-1) = s'_{i-1}(t=0)$ and $s'_i(t=1) = s'_{i+1}(t=0)$ are imposed. The loss function for s_i is formulated as

$$E_i = \|s'_i(t = -1) - s'_{i-1}(t = 0)\|_2^2 + \|s'_i(t = 1) - s'_{i+1}(t = 0)\|_2^2 \quad (11)$$

Then, the loss function for the whole curve $E = \sum_i E_i$ is determined to derive the optimal attributes for the splines. The base points corresponding to the splines of the curve are corrected by gradient descent method.

$$\begin{pmatrix} x_i^{(k+1)} \\ y_i^{(k+1)} \end{pmatrix} = \begin{pmatrix} x_i^{(k)} \\ y_i^{(k)} \end{pmatrix} + \eta \begin{pmatrix} \frac{\partial E}{\partial x_i} \\ \frac{\partial E}{\partial y_i} \end{pmatrix} \quad (12)$$

where $k+1$ and k are the number of iterations, η is the learning rate. The coordinate of the base point is iterated and updated until it converges or reaches the maximum number of iterations. Fig. 8 shows that the proposed smoothing method can eliminate the aliasing and noises on the curve while maintaining the primitive shape of the curve.

The parameters in the (10) are recalculated with the updated coordinates and then the curvature at P_i is computed as

$$\begin{aligned} \kappa_i(t) &= \frac{x'(t)y''(t) - x''(t)y'(t)}{(x'(t)^2 + y'(t)^2)^{3/2}} \\ &= \frac{2(2t \cdot a_i + b_i) \cdot c_i - 2(2t \cdot c_i + d_i) \cdot a_i}{((2t \cdot a_i + b_i)^2 + (2t \cdot c_i + d_i)^2)^{3/2}} \end{aligned} \quad (13)$$

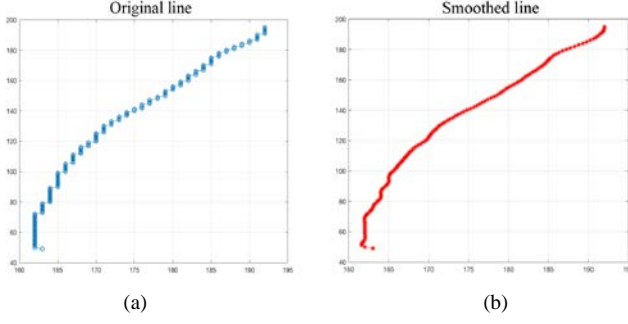


Fig. 8 The comparison between the lines without smoothness (a) and with smoothness (b)

Procedures for smoothing and curvature calculation are shown in Table 1. The curvatures of approximate 150,000 edge points in 100 images are calculated using the above algorithm. The statistical result is shown in Fig. 9.

Table 1 Smoothing and curvature calculation algorithm

Input: Edge map of human labeled image
Output: Curvatures of edge pixels
1. thin the edge map;
2. establish matrix variable <i>clist</i> , scalar variable <i>cRows</i> =1;
3. for each of the edge pixels p_0 , do
4. establish scalar variable <i>cClos</i> =1, <i>clist</i> (<i>cRows</i> , <i>cClos</i>)= p_0 ;
5. label p_0 , search eight-neighbor of p_0 ;
6. while there is an unlabeled edge pixel denoted as p_1 then
7. <i>cClos</i> = <i>cClos</i> +1, <i>clist</i> (<i>cRows</i> , <i>cClos</i>)= p_1
8. label p_1 , search eight-neighbor of p_1
9. end while
10. reverse the order of the points in <i>cRows</i> -th rows of <i>clist</i> ;
11. search again the eight-neighbor of p_0 using steps 6-9;
12. <i>cRows</i> = <i>cRows</i> +1;
13. end for
14. for each of the points in <i>clist</i> , do
15. adjust the coordinates of the points using (12);
16. calculate the curvatures with (13);
17. end for

Bringing the statistics result in Fig. 9 into (2), the \bar{m} and δ can be calculated as

$$\begin{cases} \bar{m} = \sum_i f_i m_i \\ \delta^2 = \frac{1}{n} \sum_{i=1}^n (m_i - \bar{m})^2 \end{cases} \quad (14)$$

where m_i is the change of curvature, f_i is the frequency of the occurrence of m_i .

V. CONTOUR EXTRACTION AND QUALITY INSPECTION

Based on the motion model, the proposed contour extraction method is divided into three stages. In preprocess stage, the image is firstly segmented into several ROIs based on the prior information acquired from a predefined filter. Then, a named mpb detector is adopted to detect edges in the ROIs, respectively. After that, the following two stages are conducted for each of the ROIs, respectively.

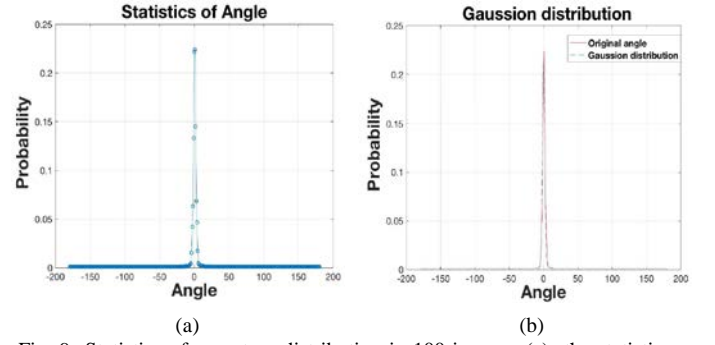


Fig. 9 Statistics of curvature distribution in 100 images. (a) the statistics result. (b) Gaussian fitting result

In connectivity modeling stage, the probabilities of the edges belonging to the contours are calculated. The calculation involves the following two steps.

Connectivity Calculation. For ease of description, the calculation of connectivity φ between edges l_1 and l_2 is taken as an example. The two endpoints of l_1 are respectively denoted as p_1 and p_2 while those of l_2 are q_1 and q_2 . Their orientations are θ_1 and θ_2 , respectively. The connectivity between p_i and q_j is computed ($i=1, 2, j=1, 2$) which is respectively denoted as $\varphi_{p_1q_1}$, $\varphi_{p_1q_2}$, $\varphi_{p_2q_1}$ and $\varphi_{p_2q_2}$. Then, φ is approximated by

$$\varphi \approx (\varphi_{p_1q_1} + \varphi_{p_1q_2} + \varphi_{p_2q_1} + \varphi_{p_2q_2})/4 \quad (15)$$

In addition, we further explain the calculation of the connectivity between edge endpoints. Without loss of generality, we take $\varphi_{p_1q_1}$ for instance. $\varphi_{p_1q_1}$ denotes the probability of a particle moving from p_1 in the direction θ_1 to p_2 heading the direction θ_2 . Based on the Brownian motion model, it is computed with (5), (6) and (7). Similarly, $\varphi_{p_1q_2}$, $\varphi_{p_2q_1}$ and $\varphi_{p_2q_2}$ can be calculated and φ is then obtained. In this way, the connectivity matrix S in which the connectivity between every two edges in the image is involved can be constructed.

Probability Determination. The probability is regarded as the path-based connectivity between the edge and the endpoint extracted in Section III. The calculation is based on the connectivity matrix S and connectivity between the endpoint and edges in the image. We consider this process as a shortest path problem in a directed graph and the Dijkstra's algorithm [24], which is an algorithm for finding the shortest paths between nodes in a graph, is adopted to solve this problem. With this method, an edge-in-contour figure in which the gray-values of the edges represent the probabilities of belonging to the contour can then be established.

In edge grouping procedure, we use the criterion SRC method [21] to implement the contour extraction. The edge-in-contour figure mentioned above is processed by binarization with a threshold T_4 and then is used as the input of the SRC. With extracted contours, the defects such as wire-lacking and wire-broken could be straightforwardly inspected. As the name suggests, wire-lacking indicates that one or more wire(s) disappeared, leading to the amount of wires less than five, while wire-broken means that fissure or deletion occurred in the wire(s). Intuitively, the defect of wire-lacking could be inspected by the amount of extracted contours, and the defect of wire-broken could be inspected by the length in the principal

orientation of the contour. With the extracted contours, we employ the following rules to inspect the two defects. If the amount is less than five, the component is wire-lacking. If the length(s) is shorter than half of the radius of the component, it should be considered as wire-broken. The entire flowchart of the contour extraction and quality inspection procedures is illustrated in Fig. 10.

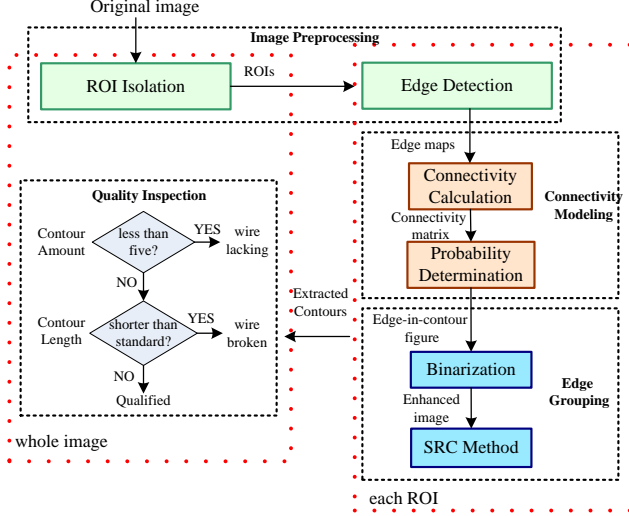


Fig. 10 The flowchart of the proposed contour extraction method

VI. EXPERIMENTS AND RESULTS

According to the configuration provided in Section II, an experimental system was set up, as shown in Fig. 11. In this experiment system, the camera was consisted of one RM17-10-000-65 endoscope and one CAM-200 CCD. The size of test image captured by the system was 768×576 . The algorithm was implemented using MATLAB code, running on a laptop computer with OS operating system, Intel Core™ i7, 3.3 GHz, and 16-GB RAM. In the extraction of wire endpoint, threshold T_1 was set to 5. For curve segmentation, threshold T_2 which represents the maximum distance between the edge and straight line was set to 2 and threshold T_3 which represents the minimum distance to be discarded was set to 5. For edge grouping, the binary threshold T_4 was set to 0.2. In the experiment, the change of angle obeyed Gaussian distribution $N \sim$

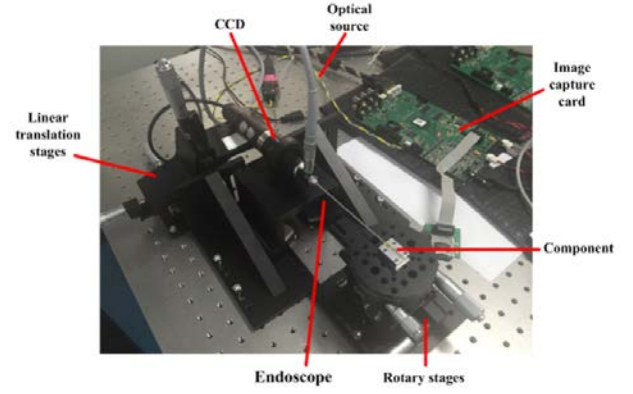


Fig. 11 Experimental system configuration

(0.083, 3.0262).

A. Contour grouping

To evaluate the proposed method quantitatively, we tested the proposed contour extraction method on real images. On the images, we firstly segmented the original image into five ROIs. Then, we constructed the detected segments by edge detection and curve segmentation. We used the mpb detector in edge detection, and SRC method in edge grouping, leaving the parameters at their default values. On the basis, the proposed method was used to group the edges on the same contour together.

For better illustration, the intermediate results in two of the experiments are shown in Fig. 12. In the figure, the first column shows the original images and their corresponding edge images, enhanced edge images and contour extraction results are shown in the second, third and fourth columns, respectively. In the fourth column in Fig. 12, yellow dashed lines and red solid lines respectively represent the contour and the skeleton of the target. It can be seen from Fig. 12(a) that the materials of the components employed in the two experiments are quite different. Besides, the sizes of the captured images are also different. The first experiment (the first row in Fig. 12) has an image size of 1280×1005 pixels while in the second experiment (the second row in Fig. 12), the image size is 768×576 pixels. Experimental results demonstrate that our method adapts to these changes and get satisfactory results.

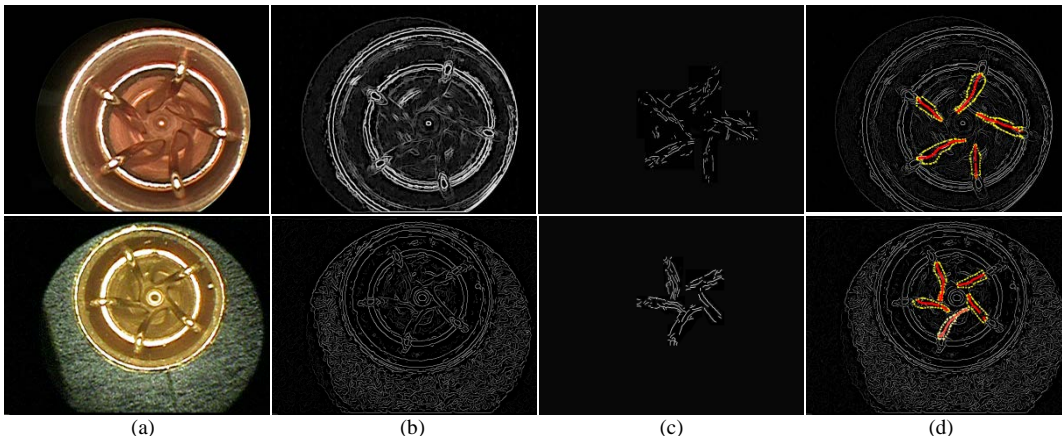


Fig. 12 Detection result. (a) original image (b) output of mPb edge detection (c) edge image enhanced by proposed method (d) contour and skeleton extracted by SRC.

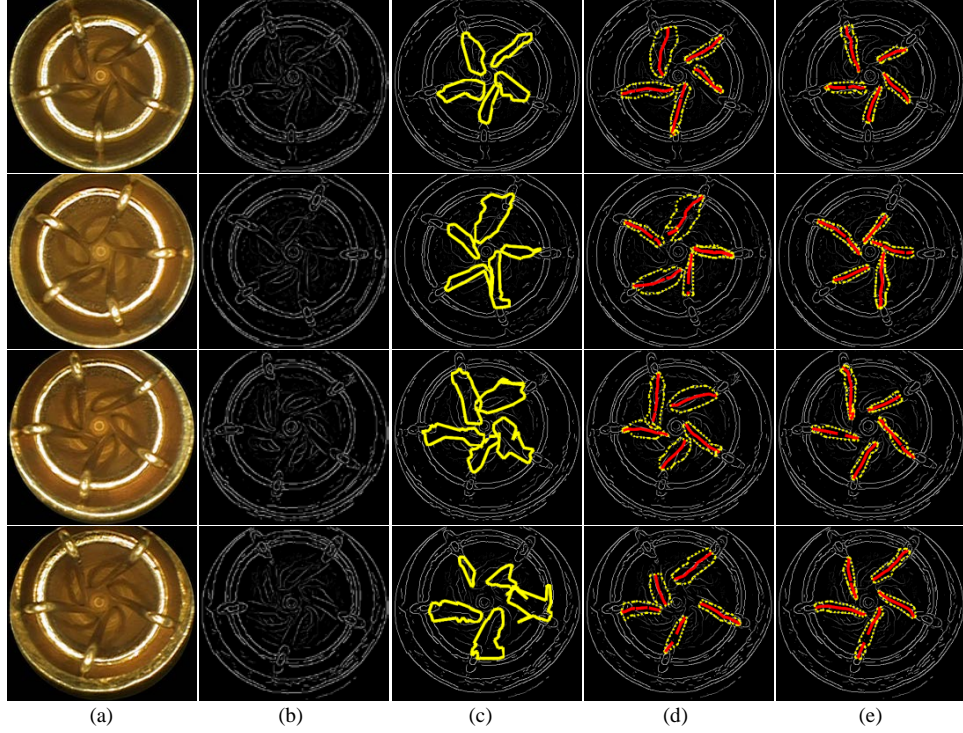


Fig. 13 Comparison results among the proposed method, the SRC method and the RRC method. (a) original image (b) output of mPb edge detection (c) contour extracted by RRC (d) contour and skeleton extracted by SRC (e) contour and skeleton extracted by the proposed method.

From the comparison of Figs. 13(b) and 13(c), we found that the edges belonging to the target contour are enhanced while most of the edges which arise from the noises and shadows are suppressed. After thresholding, the amount of the edges in the figures is decreased enormously. This leads to a significant improvement in computational efficiency while ensuring detection accuracy.

In very few cases, the algorithm can only detect the main contour of the target but cannot extract the whole contour completely. This is due to the fact that the contrast in some regions is so low that the edges are totally neglected by the detectors. But it would have little effect on the final inspection.

B. Comparison experiments

For further demonstration, comparison experiments were conducted among the proposed method with the criterion SRC method [21] and the criterion RRC method [25]. The parameters of the comparison methods are selected as their default values. Experimental results are shown in Figs. 13 and 14 where images with different scales were adopted to verify the robustness. In Fig. 13, the image size is 400×368 pixels and it is 1248×938 pixels in Fig. 14. In Figs. 13 and 14, the first and second columns are the original images and the corresponding edge images obtained with mpb detector. The third to fifth columns show the extraction results of the RRC method, the SRC method and the proposed method, respectively.

We found from the figures that the RRC method can only roughly describe the location of the target, but it cannot accurately extract the target contour due to textures. The SRC method sufficiently explores symmetry information, thus achieving superior performance over the RRC method. How-

ever, the SRC method is susceptible to noise and shadow, and sometimes cannot extract the accurate contour either. In contrast, with the consideration of prior information, the proposed method can extract contours more precisely and robustly. Besides, it also could be found from the figures that, the RRC and SRC methods could not adapt to the change in image scales. As shown in Fig. 13(c), the RRC method could roughly extract the contours of the targets in small scale images, and it performs even worse for large scale images as shown in Fig. 14(c). Unlike the RRC method, the SRC method could accurately extract the contours in large scale images as shown in Fig. 14(d), but performs poorly for small scale images as illustrate in Fig. 13(d). However, under any of the alternatives, our method performs well in extracting target contours.

Experiment demonstrates that, the proposed method occupies the capability of dealing with low-contrast, noises and shadows in the particular images, while other methods do not. Moreover, the proposed method can extract the complete morphological information of the target. Thus, it is more accurate in object representation.

C. Quality inspection

In this section, experiments were conducted to verify the effectiveness of contour-based inspection. Qualities of the components with the typical defects of wire-lacking and wire-broken were inspected. Contour extraction was performed for each component, and several of the results were provided in Fig. 15. The two columns in the figure respectively show the original images and their corresponding contour extraction results. In the first row, the length of the contour in the left is shorter than half of the radius of component. Thus, this

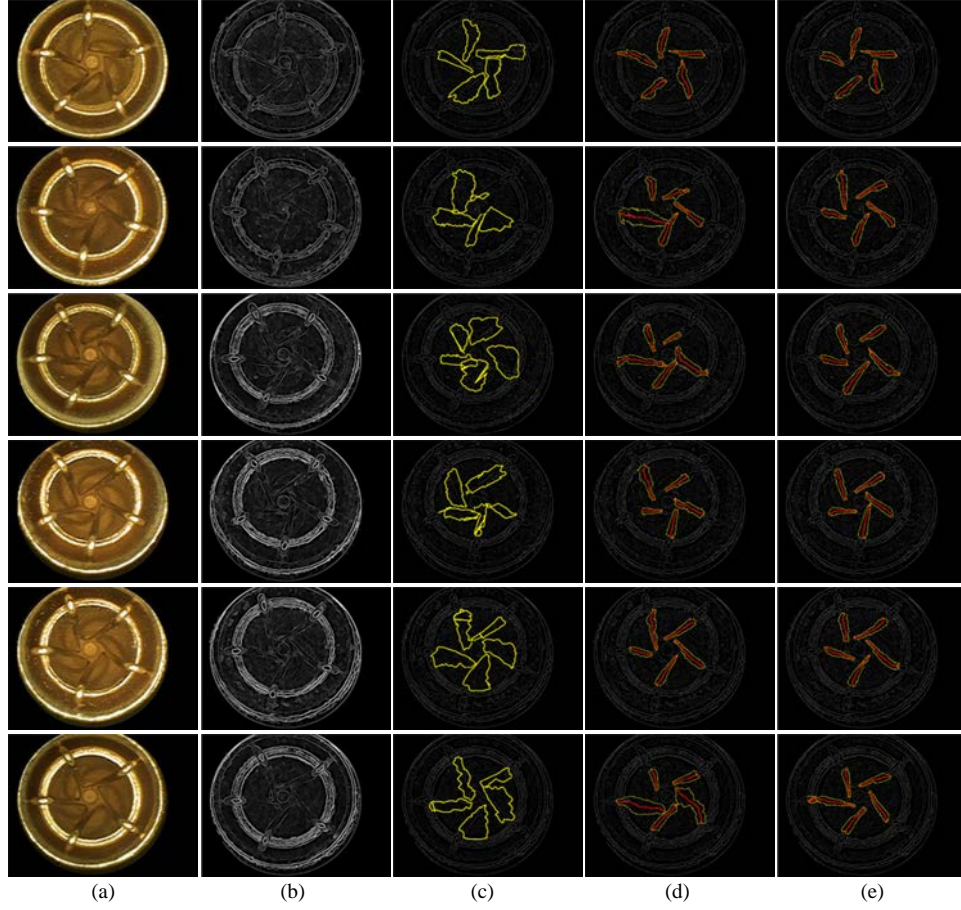


Fig. 14 Contour extraction results on other real images. (a) original image (b) output of mPb edge detection (c) contour extracted by RRC (d) contour and skeleton extracted by SRC (e) contour and skeleton extracted by the proposed method.

component is determined as wire broken. And in the other two rows, the amounts of the contours are less than five, and the components are determined as wire-lacking.

In industrial site, we statistically found that components with the defects of wire-lacking and wire-broken account for about eighty percent of all defective components. This means that, based on the contour extracted by the proposed method, a vast majority of defective components can be inspected. Therefore, we can conclude that, extracting the contours of wires precisely and robustly is crucial for effective inspection of the component. Combining contours with other types of features would certainly be helpful to further improve inspection performance.

D. Running time

The proposed Brownian motion model can enhance the edges that belong to the contour and can also suppress the other edges by calculating the connectivity of the edges. This will improve not only improve the effectiveness, but also the real-time performance of the proposed method. We tested the running time of the above three algorithms for multiple images at multiple scales. The average running time of the methods for multiple images at different scales is shown in Fig. 16. In the chart, the abscissa is the size of the image, corresponding to the length of the image times the width, and the ordinate is the running time. The blue, orange and gray lines respectively represent the proposed method, the SRC method and the RRC

method. It can be seen from Fig. 16 that, compared to the SRC

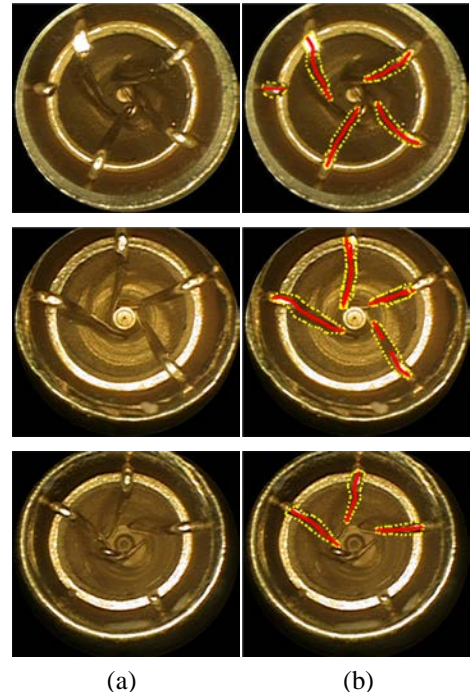


Fig. 15. Result of defect detection. (a) is the original images (b) is the result of contour extraction

method, the proposed method has greatly improved the running time for both small scale images and large scale images. For the RRC method, the proposed method reduces the running time a lot on the small-scale images. However, with the increase of the image size, the improvement effect is gradually reduced. The experiment demonstrates that the proposed algorithm can greatly improve the real-time performance of contour grouping while ensuring the effect of contour extraction.

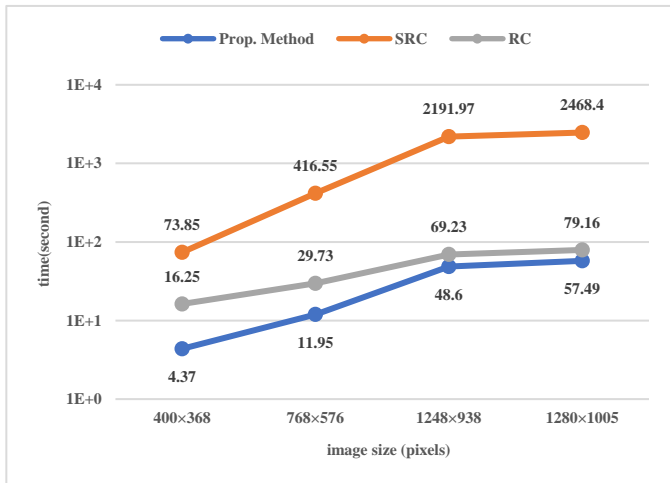


Fig. 16 Running time of the proposed method, the SRC method and the RRC method

VII. CONCLUSION

This paper presents a contour extraction method for the inner wires of the component with small diameter and deep hole. An automatic image acquisition system is developed to capture high-quality images. In the extraction of the inner wires' contours, prior information and experience data are sufficiently considered, and a curve smoothing algorithm is provided to guarantee the accuracy. Meanwhile, the named mpb operator is utilized to detect edges. A discrete Brownian motion is modeled to calculate the connectivity between the edges. On the bias, a path-based method is designed to compute the probability of the edges belonging to the contour. Experiments are implemented with the proposed method to test its performance on a set of images. Comparison experiments are also conducted to compare the performances between the proposed method and other methods. These experiments showed that the proposed method can extract the contour of component's inner structure completely and achieve high performance in terms of real-time and extraction accuracy. Furthermore, we performed a preliminary inspection of the components' quality based on the extracted contour. The experiments demonstrated that the premise of accurately inspecting the quality of component is to extract the contour precisely and robustly.

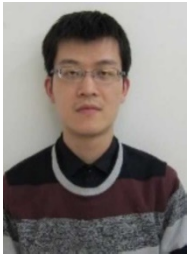
REFERENCES

- [1] X. Tao, Z. Wang, Z. Zhang, D. Zhang, D. Xu, X. Gong, L. Zhang, "Wire Defect Recognition of Spring-Wire Socket Using Multitask Convolutional Neural Networks," *IEEE Transactions on Components, Packaging and Manufacturing Technology*, vol. 8, issue. 4, pp. 689-698, 2018.
- [2] N. Cai et al., "A new IC solder joint inspection method for an automatic optical inspection system based on an improved visual background ex-

- traction algorithm," *IEEE Transactions on Components, Packaging and Manufacturing Technology*, vol. 6, issue. 1, pp. 161-172, 2016.
- [3] Q. Ye, N. Cai, J. Li, F. Li, H. Wang, X. Chen, "IC Solder Joint Inspection Based on an Adaptive-Template Method," *IEEE Transactions on Components, Packaging and Manufacturing Technology*, vol. 8, issue. 6, pp. 1121-1127, 2018.
- [4] G. Papari and N. Petkov, "Edge and line oriented contour detection: State of the art," *Image and Vision Computing*, vol. 29, no. 2, pp. 79-103, 2011.
- [5] J. Canny, "A computational approach to edge detection," *IEEE Transactions on Pattern Analysis and Machine Intelligence*, vol. PAMI-8, issue 6, pp. 679-698, 1986.
- [6] R. Martin, C. Fowlkes, and J. Malik, "Learning to detect natural image boundaries using local brightness, color, and texture cues," *IEEE Transactions on Pattern Recognition and Machine Learning*, vol. 26, no. 5, pp. 530-549, 2004.
- [7] X. Ren, "Multi-scale improves boundary detection in natural images," *European Conference on Computer Vision*, Marseille, France, 2008, pp. 533-545.
- [8] X. Ren, B. Li, "Discriminatively trained sparse code gradients for contour detection," *Advances in Neural Information Processing Systems*, Lake Tahoe, Nevada, USA, 2012, pp. 584-592.
- [9] Arbelaez P, Maire M, Fowlkes C, et al. "Contour detection and hierarchical image segmentation," *IEEE Transactions on Pattern Analysis and Machine Intelligence*, vol. 33, issue 5, pp. 898-916, 2011.
- [10] M. Maire, P. Arbelaez, C. Fowlkes, and J. Malik, "Using contours to detect and localize junctions in natural images," *IEEE Conference on Computer Vision and Pattern Recognition*, Anchorage, AK, USA, 2008, pp. 1-8.
- [11] Q. Peng, Y. Cheung, X. You, et al. A hybrid of local and global saliencies for detecting image salient region and appearance. *IEEE Transactions on Systems, Man, and Cybernetics: Systems*, vol. 47, issue 1, pp. 86-97, 2017.
- [12] P. Arbelaez, "Boundary extraction in natural images using ultrametric contour maps," *IEEE Conference on Computer Vision and Pattern Recognition*, New York, NY, USA, 2006, pp. 182-182.
- [13] P. Arbelaez, et al. "Multiscale combinatorial grouping," *IEEE Conference on Computer Vision and Pattern Recognition*, Columbus, OH, USA, 2014, pp. 328-335.
- [14] Y. Ming, H. Li, X. He, Winding number constrained contour detection. *IEEE Transactions on Image Processing*, vol. 24, issue 1, pp. 68-79, 2015.
- [15] M.A.M. Abdullah, S.S. Dlay, W.L. Woo, et al. Robust iris segmentation method based on a new active contour force with a noncircular normalization. *IEEE Transactions on Systems, Man, and Cybernetics: Systems*, vol. 47, issue 12, pp. 3128-3141, 2017.
- [16] Amir and M. Lindenbaum, "A generic grouping algorithm and its quantitative analysis," *IEEE Transactions on Pattern Analysis and Machine Intelligence*, vol. 20, issue 2, pp. 168-185, 1998.
- [17] S. Mahamud, L.R. Williams, K.K. Thornber, and K. Xu, "Segmentation of multiple salient closed contours from real images," *IEEE Transactions on Pattern Analysis and Machine Intelligence*, vol. 25, issue 4, pp. 433-444, 2003.
- [18] L. R. Williams and D. W. Jacobs, "Stochastic completion fields: A neural model of illusory contour shape and salience," *Neural Computation*, vol. 9, issue 4, pp. 837-858, 1997.
- [19] K.K. Thornber and L.R. Williams, "Analytic solution of stochastic completion fields," *Biological Cybernetics*, vol. 75, no. 2, pp. 141-151, 1996.
- [20] I.H. Jermyn and H. Ishikawa, "Globally optimal regions and boundaries as minimum ratio weight cycles," *IEEE Transactions on Pattern Analysis and Machine Intelligence*, vol. 23, issue 10, pp. 1075-1088, 2001.
- [21] S. Wang, T. Kubota, J.M. Siskind, and J. "Wang, Salient closed boundary extraction with ratio contour," *IEEE Transactions on Pattern Analysis and Machine Intelligence*, vol. 27, issue 4, pp. 546-561, 2005.
- [22] J.S. Stahl and S. Wang, "Globally optimal grouping for symmetric closed boundaries by combining boundary and region information," *IEEE Transactions on Pattern Analysis and Machine Intelligence*, vol. 30, issue 3, pp. 395-411, 2008.
- [23] Fischer and J.M. Buhmann, "Path-based clustering for grouping of smooth curves and texture segmentation," *IEEE Transactions on Pattern Analysis and Machine Intelligence*, vol. 25, issue 4, pp. 513-518, 2003.
- [24] E. W. Dijkstra, "A note on two problems in connexion with graphs," *Numerische mathematic*, vol. 1, issue 1, pp. 269-271, 1959.
- [25] J.S. Stahl, S. Wang, "Edge grouping combining boundary and region information," *IEEE Transactions on Image Processing*, vol. 16, issue 10, pp. 2590-2606, 2007.



Xinyi Gong received the B. Sc. degree in automation from Tsinghua University, Beijing, China, in 2014. He is currently working toward Ph. D degree in control science and engineering from the Institute of Automation, Chinese Academy of Sciences, Beijing, China; University of the Chinese Academy of Sciences, Beijing, China. His current research interests include computer vision, image processing, and machine learning.
ORCID iD: 0000-0002-6515-2836



Hu Su received the B. Sc. and M. Sc. Degrees in information and computation science from Shandong University, Jinan, China, in 2007 and 2010, respectively, and the Ph. D. degree in control science and engineering from the State Key Laboratory of Management and Control for Complex Systems, Institute of Automation, Chinese Academy of Sciences (IACAS) Beijing, China, in 2013. Since 2013, he has been with the IACAS, Beijing, China, where he is currently a Associate Researcher in the Research Center of Precision Sensing and Control. His current research interests include intelligent control and optimization, and computer vision.



De Xu (M'05–SM'09) received the B.Sc. and M.Sc. degrees from the Shandong University of Technology, Jinan, China, in 1985 and 1990, respectively, and the Ph.D. degree from Zhejiang University, Hangzhou, China, in 2001, all in control science and engineering. Since 2001, he has been with the Institute of Automation, Chinese Academy of Sciences, Beijing, China, where he is currently a Professor with the Research Center of Precision Sensing and Control. His current research interest includes robotics and automation, such as visual measurement, visual control, intelligent control, visual positioning, microscopic vision, and micro-assembly.
ORCID iD: 0000-0002-7221-1654



Huabin Yang received the he B.Eng. de. Degree from Shandong University of Technology, Zibo, China, in 2010, and the Ph. D. degree from CIOMPCAS, Changchun, China, in 2015, all in Mechanical manufacture and Automation Major. He is a research assistant professor in the Research Center of Precision Sensing and Control, IACAS. His research interests include optics and precision mechanics, visual measurement, and automation.
ORCID iD: 0000-0001-9955-0560



Zhengtao Zhang received the B. Sc. degree from China University of Petroleum, Dongying, China, in 2004, and M. Sc. degree from Beijing Institute of Technology, Beijing, China, in 2007, and the Ph. D. degree from IACAS, Beijing, China, in 2010, all in control science and engineering. He is a Professor in the Research Center of Precision Sensing and Control, IACAS. His research interests include visual measurement, micro-assembly, and automation.



Lei Zhang received the B.Sc. degree in mechanical and automotive engineering from the China University of Geosciences, Beijing, China. He is currently a Mechanical Engineer with the Research Center of Precision Sensing and Control, Institute of Automation, Chinese Academy of Sciences, Beijing. His current research interests include mechanical design and mechanical analysis.